JOURNAL OF COMPUTATIONAL PHYSICS **133,** 56–74 (1997)
ARTICLE NO. CP975646

A Parallel Three-Dimensional Computational Aeroacoustics Method Using Nonlinear Disturbance Equations

Philip J. Morris, Lyle N. Long, Ashok Bangalore, and Qunzhen Wang

Department of Aerospace Engineering, The Pennsylvania State University, University Park, Pennsylvania 16802

Received May 28, 1996; revised December 16, 1996

This paper describes the application of a three-dimensional computational aeroacoustics (CAA) methodology to the prediction of jet noise. The technique has been implemented using parallel computers. In this approach the nonlinear disturbance equations are solved in a conservative form using a finite-difference based technique. A fourth-order optimized dispersion relation preserving scheme is used for spatial discretization and a fourth-order classical Runge–Kutta scheme is employed for temporal discretization. The three-dimensional CAA code has been parallelized using a domain decomposition strategy in the streamwise direction. The calculations are carried out on both IBM-SP2 and SGI Power-Challenge parallel computers using message passing interface routines to facilitate exchange of boundary data between adjacent nodes (processors). Excellent parallel performance has been obtained using the present code. Acoustic results are presented for a perfectly expanded supersonic axisymmetric jet under harmonic and random inlet conditions. Results are given for both the instantaneous and averaged flow and acoustic variables. Comparisons are made between the predictions and experimental data.

1. INTRODUCTION

Previous approaches to the prediction of jet mixing noise have centered on applications of Lighthill's acoustic analogy [1], its extensions by Lilley [2], or instability wave analyses for supersonic jets (Morris and Tam [3], Tam and Burton [4]). Only in the last cases, is an attempt made to link the unsteady flow properties directly to the radiated noise. All these approaches rely to some extent on empirical inputs and their extension to jet nozzles with noncircular geometries is problematic. In this paper we introduce a formulation of the jet noise problem that takes advantage of previous developments in the prediction of the time-averaged properties of jet flows as well as the power of high performance computers to predict their unsteady characteristics, including the radiated noise.

Computational Aeroacoustics (CAA) has received a great deal of attention in recent years. The goal of CAA is the development of a numerical methodology to predict the noise characteristics of fluid flows under different conditions. Even though the numerical approaches have some similarities to those used in traditional CFD techniques, the nature of the problems addressed and the results desired are very different in the case of CAA studies. Some of the critical issues that are typical of CAA are: the nondissipative and nondispersive character of acoustic waves; the extremely low amplitude of acoustic perturbations compared to the mean flow values; and the high frequencies of waves that need to be resolved. Hence special attention has to be given in the development of numerical techniques to address these issues, particularly the minimization of dissipative and dispersive errors. The following section gives a brief review of current CAA methods used in jet noise predictions.

Hixon *et al.* [5] used a solution of the linearized Euler equations to predict the jet noise characteristics of an axisymmetric supersonic jet. Analytic mean flow profiles were specified in their calculations. A large eddy simulation (LES) approach was used by Mankbadi *et al.* [6] to simulate the near field characteristics of supersonic jets. They used an acoustic analogy to compute the far-field noise. Chyczewski and Long [7] used a sixth-order full 3D Navier–Stokes method to simulate the noise generation mechanisms in high speed jets. In their study, they predicted the flapping motion and the axis-switching of a rectangular jet successfully. A Kirchhoff integral method was used to predict the far-field noise. Mitchell *et al.* [8] used a 2D direct numerical simulation (DNS) of the compressible Navier–Stokes equations to predict the flow and noise characteristics of subsonic and supersonic jets. They used a fourth-order Padé scheme but performed only two-dimensional axisymmetric simulations. Recently, Viswanathan and Sankar [9] used a fluid/acoustic coupled approach to predict noise radiated from axisymmetric supersonic jets. They used a two–four MacCormack scheme for the acoustic calculations and a hybrid implicit Navier–Stokes solver to calculate the mean flow solution. Their calculations were also restricted to two-dimensional axisymmetric simulations.

The present method takes advantage of numerical developments in the solution of both the Reynolds-averaged

0021-9991/97 $25.00

Navier–Stokes (RANS) equations and CAA methodologies. Variables are split into a mean component, that satisfies the RANS equations and a perturbation about that mean. The mean component is obtained from a numerical solution of the RANS equations, with a simple algebraic turbulence model, using a traditional, robust CFD algorithm with good convergence characteristics. Although such algorithms provide solutions of the time-averaged equations, they are incapable of capturing the time-accurate characteristics of the unsteady flow field and the nondispersive and nondissipative characteristics of the acoustic fields. These unsteady properties are obtained using a CAA methodology for the perturbations about the mean flow. The complete equations for the perturbations, called here the nonlinear disturbance equations, consist of linear and nonlinear fluctuation terms, spatially varying coefficients that depend on the mean flow properties, and a mean-flow source term that is independent of the fluctuations. The only simplifying assumption made is that the disturbances are essentially inviscid in nature. This is certainly true for the acoustic field and is also a good approximation for the large scale turbulent structures, which are mostly responsible for the noise radiation in high speed jets and are the only scales resolved in the present simulations. There are several advantages to the decomposition used here. Since the magnitude of the instantaneous properties in the unsteady flow are several orders of magnitude larger than the acoustic fluctuations, numerical round-off errors affecting the acoustic solution are reduced. Boundary treatments may be used, both radiation and outflow conditions, that have been developed for perturbation quantities and applied successfully in CAA applications. However, the significant advantage of the present approach is that algorithms are used that are best suited to the decomposed equations: traditional CFD algorithms for the mean flow and CAA algorithms for the unsteady flow and acoustic perturbations.

A noise prediction method, described by Hardin and Pope [10, 11], also splits the instantaneous properties of the flow. However, their methodology is quite different from the present scheme. First, they assume that the acoustic sources at low Mach numbers may be obtained from an unsteady solution of the two-dimensional, incompressible, Navier–Stokes equations. They then argue that, although the flow is incompressible, there will be small density perturbations associated with the pressure perturbations, and they are obtained by making an isentropic assumption. Finally, the acoustic properties are regarded as perturbations about the incompressible solution that satisfy the compressible equations of motion. The philosophical approach taken by this method is similar to the present scheme: to solve systems of equations that describe the various components of the flow using different techniques. However, it is best suited to low Mach number flows, the unsteady source solution is laminar, and all calculations are two-dimensional. The decomposition strategy introduced in the present paper, as well as the use of a parallel numerical implementation, allows a full three-dimensional simulation of both the unsteady flow and noise of a supersonic jet to be performed.

The rest of the paper is organized as follows. First, the nonlinear disturbance equations are developed. Next, the numerical algorithms for the mean flow and the perturbation equations are explained, along with the boundary conditions. Then, parallel performance issues are discussed. Three-dimensional, time-dependent, code validation results are presented next. Circular jet flow and acoustic results are then presented and compared with experimental data.

2. GOVERNING EQUATIONS

The nonlinear disturbance equations (NDE) are obtained from the conventional Reynolds decomposition of the full, time-dependent Navier–Stokes equations. The three-dimensional Navier–Stokes equations in a Cartesian coordinate system may be written in the form [12]

$$\frac{\partial q}{\partial t}+\frac{\partial F}{\partial x}+\frac{\partial G}{\partial y}+\frac{\partial H}{\partial z}=\frac{\partial R}{\partial x}+\frac{\partial S}{\partial y}+\frac{\partial E}{\partial z}. \tag{1}$$

The conserved variable vector is given by

$$q=\begin{Bmatrix}\rho\\ \rho u\\ \rho v\\ \rho w\\ e\end{Bmatrix}, \tag{2}$$

where ρ is the fluid density and u, v, w are velocity components in the three coordinate directions, respectively. The total energy per unit volume of fluid is defined as

$$\begin{aligned} e&=\rho\left[C_vT+\frac{1}{2}(u^2+v^2+w^2)\right]\\ &=\frac{p}{\gamma-1}+\frac{1}{2}\rho(u^2+v^2+w^2), \end{aligned} \tag{3}$$

where p, T, C_v, and γ are the pressure, temperature, constant volume specific heat, and specific heat ratio, respectively. Note that, in Eq. (3), the ideal gas law is used to

relate pressure and temperature. The inviscid flux terms in Eq. (1) are given by

$$F = \begin{Bmatrix} \rho u \\ \rho u^2 + p \\ \rho uv \\ \rho uw \\ (e+p)u \end{Bmatrix} \tag{4}$$

$$G = \begin{Bmatrix} \rho v \\ \rho uv \\ \rho v^2 + p \\ \rho vw \\ (e+p)v \end{Bmatrix}. \tag{5}$$

$$H = \begin{Bmatrix} \rho w \\ \rho uw \\ \rho vw \\ \rho w^2 + p \\ (e+p)w \end{Bmatrix} \tag{6}$$

while R, S, and E are the viscous stresses in the three coordinate directions, respectively [12].

To derive the nonlinear disturbance equations, the flow vector q is split into its mean value q_o and a perturbation q'

$$q = q_o + q', \tag{7}$$

where

$$q_o = \lim_{T\to\infty} \frac{1}{T} \int_{t_0}^{t_0+T} q(t)\, dt \tag{8}$$

and the flow is assumed to be statistically stationary. Substitution of Eq. (7) into Eq. (1) results in a set of perturbation fluxes and corresponding mean flow flux terms. By definition, the mean flow is independent of time and the only time derivative appearing in the equation set is that of the perturbation flow vector. The flux terms involving the perturbation quantities are retained on the left-hand side and the terms involving purely mean flow quantities are treated as source terms (on the right-hand side). The perturbation flux terms also contain nonlinear perturbation quantities. The viscous perturbation terms are neglected, as it is argued, following Hardin and Pope [10, 11], that the time-average properties are the result of dissipative mechanics, whereas the large-scale fluctuations are essentially inviscid in nature. After rearrangement of the mean flow and perturbation terms as well as neglect of the viscous perturbation terms, the nonlinear disturbance equations in Cartesian form can be written as

$$\frac{\partial q'}{\partial t} + \frac{\partial F'}{\partial x} + \frac{\partial G'}{\partial y} + \frac{\partial H'}{\partial z} + \frac{\partial F'_n}{\partial x} + \frac{\partial G'_n}{\partial y} + \frac{\partial H'_n}{\partial z} = Q, \tag{9}$$

where

$$q' = \begin{Bmatrix} \rho' \\ \rho_o u' + \rho' u_o + \rho' u' \\ \rho_o v' + \rho' v_o + \rho' v' \\ \rho_o w' + \rho' w_o + \rho' w' \\ e' \end{Bmatrix} \tag{10}$$

$$F' = \begin{Bmatrix} \rho_o u' + \rho' u_o \\ \rho' u_o^2 + 2\rho_o u_o u' + p' \\ \rho_o u_o v' + \rho_o v_o u' + \rho' u_o v_o \\ \rho_o u_o w' + \rho_o w_o u' + \rho' u_o w_o \\ u'(e_o + p_o) + u_o(e' + p') \end{Bmatrix} \tag{11}$$

$$G' = \begin{Bmatrix} \rho_o v' + \rho' v_o \\ \rho_o v_o u' + \rho_o u_o v' + \rho' u_o v_o \\ \rho' v_o^2 + 2\rho_o v_o v' + p' \\ \rho_o v_o w' + \rho_o w_o v' + \rho' v_o w_o \\ v'(e_o + p_o) + v_o(e' + p') \end{Bmatrix} \tag{12}$$

$$H' = \begin{Bmatrix} \rho_o w' + \rho' w_o \\ \rho_o w_o u' + \rho_o u_o w' + \rho' u_o w_o \\ \rho_o w_o v' + \rho_o v_o w' + \rho' w_o v_o \\ \rho' w_o^2 + 2\rho_o w_o w' + p' \\ w'(e_o + p_o) + w_o(e' + p') \end{Bmatrix} \tag{13}$$

and

$$F'_n = \begin{Bmatrix} \rho' u' \\ 2\rho' u' u_o + \rho_o u'^2 + \rho' u'^2 \\ \rho_o u' v' + \rho' v' u_o + \rho' u' v_o + \rho' u' v' \\ \rho_o u' w' + \rho' w' u_o + \rho' u' w_o + \rho' u' w' \\ u'(e' + p') \end{Bmatrix} \tag{14}$$

$$G'_n = \begin{Bmatrix} \rho' v' \\ \rho_o u' v' + \rho' v' u_o + \rho' u' v_o + \rho' u' v' \\ 2\rho v' v_o + \rho_o v'^2 + \rho' v'^2 \\ \rho_o v' w' + \rho' w' v_o + \rho' v' w_o + \rho' v' w' \\ v'(e' + p') \end{Bmatrix} \quad (15)$$

$$H'_n = \begin{Bmatrix} \rho' w' \\ \rho_o u' w' + \rho' w' u_o + \rho' u' w_o + \rho' u' w' \\ \rho_o v' w' + \rho' w' v_o + \rho' v' w_o + \rho' v' w' \\ 2\rho w' w_o + \rho_o w'^2 + \rho' w'^2 \\ w'(e' + p') \end{Bmatrix}. \quad (16)$$

The linear convective fluxes involving the perturbation quantities are F', G', and H', whereas F'_n, G'_n, and H'_n are the nonlinear perturbation terms in the three coordinate directions. The mean flow source term Q in Eq. (9) may be written as

$$Q = -\left(\frac{\partial F_o}{\partial x} + \frac{\partial G_o}{\partial y} + \frac{\partial H_o}{\partial z}\right) + \frac{\partial R_o}{\partial x} + \frac{\partial S_o}{\partial y} + \frac{\partial E_o}{\partial z}, \quad (17)$$

where the mean convective fluxes are given by

$$F_o = \begin{Bmatrix} \rho_o u_o \\ \rho_o u_o^2 + p_o \\ \rho_o u_o v_o \\ \rho_o u_o w_o \\ u_o(p_o + e_o) \end{Bmatrix} \quad (18)$$

$$G_o = \begin{Bmatrix} \rho_o v_o \\ \rho_o u_o v_o \\ \rho_o v_o^2 + p_o \\ \rho_o v_o w_o \\ v_o(p_o + e_o) \end{Bmatrix} \quad (19)$$

$$H_o = \begin{Bmatrix} \rho_o w_o \\ \rho_o u_o w_o \\ \rho_o v_o w_o \\ \rho_o w_o^2 + p_o \\ w_o(p_o + e_o) \end{Bmatrix}. \quad (20)$$

The mean viscous stresses R_o, S_o, and E_o can be obtained by simply replacing the instantaneous quantities (u, v, w, T) in the definition of R, S, and E by their corresponding mean value (u_o, v_o, w_o, T_o). Here ρ', p', u', v', w', and e' are the perturbation density, pressure, velocity components, and total energy, respectively, while their corresponding mean quantities are ρ_o, p_o, u_o, v_o, w_o, and e_o. After the conservative perturbation variable q' is obtained from the solution of Eq. (9), the velocity perturbations u', v', and w' may be obtained from q' and the mean flow values using Eq. (10), while the fluctuating pressure p' may be obtained from

$$e' = \frac{p'}{(\gamma - 1)} + (\rho_o + \rho')(u' u_o + v' v_o + w' w_o) + \frac{1}{2}(\rho_o + \rho')(u'^2 + v'^2 + w'^2) + \frac{1}{2}\rho'(u_o^2 + v_o^2 + w_o^2).$$

As noted above, the disturbance viscous flux terms are neglected in Eq. (9) for the present free shear flow simulation. However, for bounded shear flows both the linear and nonlinear disturbance viscous flux terms would need to be included.

The source term Q is essentially the sum of the divergence of mean convective fluxes and the mean viscous stresses. If Eq. (9) is time averaged, it becomes the Reynolds averaged Navier–Stokes equations. The left-hand side would yield the Reynolds stress terms. The term Q could be replaced by the Reynolds stress terms from the RANS equations and for a laminar flow $Q = 0$. In the present work, the mean-flow quantities are obtained from a separate solution of the Reynolds averaged Navier–Stokes equations [9], and the unknown perturbation quantities are obtained from the time-dependent nonlinear disturbance equations.

A final simplifying assumption is made in the present implementation which prevents the scheme from being a full closure of the unsteady flow and noise problem at this time. The mean-flow source terms in the nonlinear disturbance equations are neglected. Previous predictions, based on instability wave models [3, 4], have shown that the flow and acoustic mechanisms are weakly nonlinear in nature. If the problem were completely linear, it is readily shown that the unsteady solution of a hyperbolic problem is independent of time-independent source terms. The solution is dominated by the unsteady properties of the boundary conditions. This is expected to be the case in the high speed jets simulated in the present paper. Thus, the present simulation determines the absolute amplitude of the radiated noise by matching against experimental data at a single point in the far field. There are two primary reasons for this. Since the mean flow source terms involve derivatives of mean fluxes it is important that the mean

flow solution be sufficiently smooth. It was found that the mean flow solution used in the present calculations had some unrealistic derivatives, especially in the initial region of the jet. This might have been due to incomplete convergence or the relatively low spatial order of the scheme. Second, the introduction of the source terms into the unsteady numerical solution can cause instabilities as a finite time is required for the numerical solution, initiated at the exit to influence the entire computational domain. Until that time there are no unsteady fluctuations to balance their time-averaged values given by the mean-flow source terms. Both these difficult computational issues are being addressed by the authors. However, the present calculations focus on supersonic jet simulations. In a complete closure the amplitude of the fluctuations would be determined by comparing the turbulence statistics obtained from the RANS equations with averages of the unsteady solution. This would also enable corrections to be made to the turbulence model approximations to the Reynolds stresses and an iterative procedure could be visualized that provided an improved turbulence closure. However, this is not the focus of the present paper which is concerned with three-dimensional predictions of the noise radiated by artificially and naturally excited supersonic jets.

3. NUMERICAL FEATURES

3.1. Mean-Flow Algorithm

The mean-flow quantities are calculated by a solution of the Reynolds averaged Navier–Stokes (RANS) equations [9]. A third-order Roe upwind scheme is used to calculate the inviscid fluxes in a finite volume approach. The viscous stresses are calculated using a standard central difference scheme. The RANS equations are solved in a time-dependent manner until a steady state is obtained. A hybrid implicit scheme is used to march the mean flow solution in time. The base solver has been validated for a variety of flow solutions and, in particular, jet flow calculations [9]. In this hybrid approach, the axial and the radial flux terms are treated implicitly while the azimuthal flux terms are calculated explicitly. The Reynolds stresses are modeled using either an algebraic turbulence model or a two-equation k-ε turbulence model. The mean flow solutions obtained in this work use the Baldwin–Lomax algebraic turbulence model. Reference [9] gives a more detailed explanation of the mean flow solution procedure.

3.2. Aeroacoustics Algorithm

The nonlinear disturbance equations are cast in a generalized coordinate system and solved numerically using a finite-difference-based scheme. The velocities are scaled with the ambient speed of sound. The density is normalized with the ambient density and the pressure is scaled with the ambient pressure. The jet radius, R_j, is used as the length scale. The discretized equations are solved in a time accurate manner using a fourth-order Runge–Kutta method. Some improvements in performance, although not accuracy, could be achieved through the use of an optimized low-dissipation low-dispersion Runge–Kutta (LDDRK) scheme [13]. The spatial flux derivatives are calculated using the fourth-order optimized dispersion relation preserving (DRP) scheme of Tam and Webb [14]. The DRP scheme used in this work uses a seven-point stencil. Tam [15] has shown that the fourth-order optimized DRP scheme has better dispersion characteristics than the standard sixth-order central difference scheme on a uniform Cartesian grid. In the present work the DRP coefficients are used to calculate the flux derivatives in the computational domain. The present CAA solver has the option of using either the DRP coefficients or the standard sixth-order central difference coefficients to calculate the spatial flux derivatives. A constant coefficient sixth-order artificial dissipation is added to damp out spurious short waves. The coefficient of dissipation is chosen to be $\frac{1}{256}$. The order of dissipation is reduced near the boundaries.

In a typical jet noise computational domain, radiation boundary conditions need to be imposed at the far-field boundaries and outflow conditions have to be imposed at the downstream boundary. The outflow boundary condition is only used when the mean flow Mach number is larger than 0.05. The inflow conditions are prescribed at the nozzle exit plane, depending on the type of excitation selected. That is, the inflow boundary condition gives the values in the first $y - z$ plane while the values in the second and third planes are obtained from neighboring planes using a standard sixth-order finite difference scheme. No radiation boundary condition is used for the nozzle exit plane since the properties at all points in this plane are determined from the inflow boundary conditions (see Section 5.3). In this work, the nonreflecting radiation conditions proposed by Tam and Webb [14] are applied at the radiation boundaries. These are similar to the radiation conditions proposed by Bayliss and Turkel [16]. At the outflow boundary, the asymptotic solutions of the linearized Euler equations are applied. These asymptotic solutions were given by Tam and Webb [14] for uniform and weakly nonuniform mean flows. They have been applied successfully to many test problems. The boundary equations are solved for the primitive perturbation variables. A three-point boundary zone is used at the radiation and the outflow boundaries. A one-sided fourth-order spatial difference scheme is used to calculate the spatial derivatives and the primitive variables are marched in time using the fourth-order Runge–Kutta method. Since polar grids are used for the circular jet calculations, the centerline of the grid at zero radius becomes a singularity. The flow variables at the centerline are obtained by azimuthal aver-

aging. This centerline treatment has been studied in detail by Shih *et al.* [17] who have shown that the azimuthal averaging is robust and does not create artificial numerical sources near the centerline. Harmonic and random excitations are prescribed at the nozzle exit plane and they are described in detail in Section 5.3. All these boundary conditions are applied at each Runge–Kutta stage of the time-marching process.

4. PARALLEL PERFORMANCE

In order to reduce the computational time, the calculations are performed in parallel using a domain decomposition strategy. Both the IBM SP2 and SGI Power Challenge have been used to develop and test the parallel code. The parallel code uses message passing interface (MPI) routines to facilitate exchange of data between different nodes (processors). Efficient parallel computations have been achieved by using the domain decomposition strategy. In this approach, the computational domain of the circular jet is divided into several grid blocks in the axial direction. Each grid block of data is processed in parallel using one node. In order to update the solution at the boundaries of a grid block, data is needed from adjacent blocks. This boundary (or interface) information is passed between adjacent grid blocks during every time step of the solution process. In order to achieve efficient parallel computation, the domain is divided in such a way as to minimize the communication time between the nodes. The grid points are divided equally among different nodes. All nodes are similar in terms of their memory and processor speeds.

Parallel performance of the present three-dimensional CAA code has been evaluated using the IBM-SP2 platform. The CPU time per grid point per time step is a good measure of the throughput of the code. The scalability of the algorithm is addressed by linearly scaling the number of processors and the total grid size. In other words, the grid size on each processor is held constant. In the present decomposition strategy, the communication takes place between the neighboring nodes only. Hence, intuitively, the total number of nodes should not affect the communication time. However, there is additional bookkeeping involved in the communication process. Such a scalability study would indicate the degradation of the performance, if any, with the increase in the global grid size. For a perfectly scalable algorithm, an increase in the number of nodes should not increase the CPU time per time step for a fixed number of grid points on each processor. Figure 1 shows the CPU time versus the number of processors, where 63,000 grid points are assigned to each processor. As seen clearly in Fig. 1, nearly constant CPU time is obtained using the present parallel CAA code.

Another measure of the efficiency of a parallel algorithm is the speedup of the computation with the number of processors with the total number of grid points held constant (i.e., the number of points on each processor decreases with increasing the number of nodes). The speedup of the parallel computation is defined as

$$\text{speedup} = \frac{\text{wall-clock time using one processor}}{\text{wall-clock time using N processors}}. \quad (21)$$

The speedup with the number of processors for the present code is shown in Fig. 2, which indicates that the wall-clock time decreases nearly linearly with the increase in number of processors. This is possible because the communication time per time step in the present algorithm is a very small

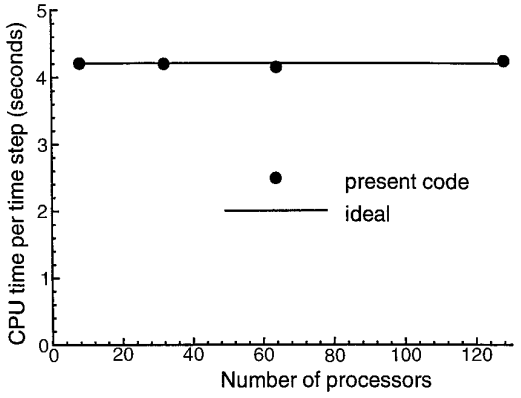

FIG. 1. CPU time per time step versus number of processors with a fixed number of grid points in each processor (i.e., the total number of grid points increases with increasing number of nodes).

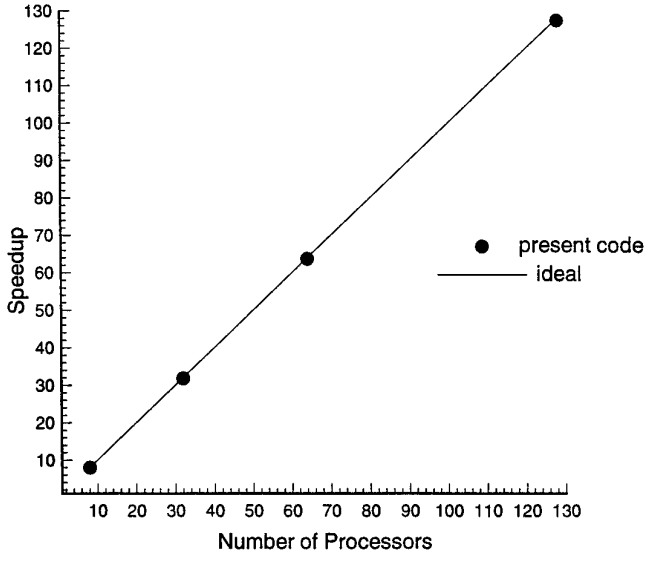

FIG. 2. Speedup versus number of processors with a fixed total number of grid points (i.e., the number of grid points in each node decreases with increasing number of processors).

fraction of the computation time. Furthermore, the communication network of the SP2 platform has a high bandwidth and a low latency. The three-dimensional supersonic jet noise results presented in this paper have been calculated using a maximum of 32 nodes. The timing calculations shown in Figs. 1 and 2 demonstrate that the present parallel CAA code is capable of solving practical large-scale aeroacoustic problems efficiently using present day parallel machines. This would otherwise not be possible in reasonable computation times using scalar computers.

4.1. Code Validation

Several three-dimensional validation problems have been solved using the present CAA code running on the IBM-SP2 and SGI Power Challenge processors. The first test case is a spherical acoustic pulse in a stationary medium while the second one is a spherical pulse in a moving medium. While these test cases do not test the nonlinear properties of the code, they do test the radiation and outflow boundary conditions and the code's temporal and spatial discretization accuracy.

4.1.1. *Spherical Acoustic Pulse in a Stationary Medium*

The pulse problem, being an initial value problem, is solved by prescribing the initial conditions in pressure and density at the center (0, 0, 0) of the computational domain. A Gaussian distribution in pressure and density is chosen as the initial distribution for the pulse and is given by

$$p', \rho' = 0.01 \exp\left[-\frac{x^2 + y^2 + z^2}{9}(\ln 2)\right]. \qquad (22)$$

The time step used in this test problem is 0.005 and a total of 20,000 steps are calculated. The computational grid is a polar grid with uniform spacing in all three directions. The grid size is $60 \times 60 \times 60$ and the computational domain is $-30 \le x \le 30$, $0 \le r \le 30$, and $0 \le \theta \le 2\pi$. This domain is divided into four subdomains in the x-direction. Each subdomain consists of $15 \times 60 \times 60$ points. The number of subdomains corresponds to the number of processors used in the simulation. The nonlinear disturbance equations (NDE) are solved in parallel in each subdomain. At each intermediate stage of the Runge–Kutta time integration, the necessary boundary information is passed between the computing nodes using MPI calls. The far-field boundary conditions are given by the Tam and Webb [14] radiation conditions.

The instantaneous acoustic pressure distributions in the streamwise direction along the centerline at different time steps are shown in Fig. 3. It is clear that the computed solution matches very well with the exact analytic solution at all time steps. At $t = 25$ (i.e., the pulse has traveled 25 units at the ambient speed of sound), the disturbance has partially exited the computational domain. At 35 time units, most of the disturbance has exited the domain, whereas all of the disturbance has exited the domain at $t = 50$. The solution shows no visible reflections from the boundaries at later times.

Figure 4 shows the average magnitude of the pressure fluctuation, $\langle |p'| \rangle$, as well as the average error in pressure, $\langle |p' - p'_{\text{exact}}| \rangle$, where p'_{exact} is the analytical solution for the pressure disturbance and $\langle\ \rangle$ denotes average over all grid points in the computational domain. Note that, at later times after all the disturbance has exited the computational domain, these two average values are identical since $p'_{\text{exact}} = 0$ everywhere in the domain. The average error shown in Fig. 4 is very small ($<10^{-7}$) at very early times (i.e., $t < 1$) but increases to $\mathcal{O}(10^{-6})$ at later times due to the artificial dissipation added in order to make the high-order code stable. Furthermore, the magnitude of the pressure disturbance does not increase significantly after the pulse moves out of the domain, indicating the wave reflection from the boundary is very small.

4.1.2. *Spherical Acoustic Pulse in a Moving Medium*

For the case of a spherical acoustic pulse in a moving medium, the grid is identical to that described in the previous, no-flow case. Initial conditions for the acoustic pulse are prescribed at the center of the computational domain (0, 0, 0) by Eq. (22). Then the disturbance equations are solved using the parallel CAA code and the spherical acoustic wave is tracked in time. A time step of 0.005 is used and a total of 26,000 steps are calculated. The mean flow Mach number is 0.5 in the x-direction. Radiation conditions are used at the far-field boundaries and the outflow boundary conditions proposed by Tam and Webb [14] are used at the downstream boundary.

Figure 5 shows the instantaneous pressure distributions in the x-direction for $y = z = 0$ at different times. Due to convection, the disturbance travels in the downstream direction and, as a consequence, the pulse first exits the computational domain through the right boundary ($x = 30$) and last exits through the left boundary ($x = -30$). It is evident from Fig. 5 that the computed pressure agrees well with the exact solution, even at later times. At $t = 20$, the disturbance has partially exited the computational domain through the right boundary and the center of the pulse moves to the right boundary at $t = 30$. After that, the pulse begins to move out of the computational domain through the right boundary and at $t = 50$ part of the disturbance has exited the left boundary whereas all of the disturbance has exited the entire domain at $t = 100$. The cross-sectional acoustic pressure contours at 25 and 50 time units are shown in Fig. 6. Note that a significant portion of the acoustic wave has exited the outflow boundary at

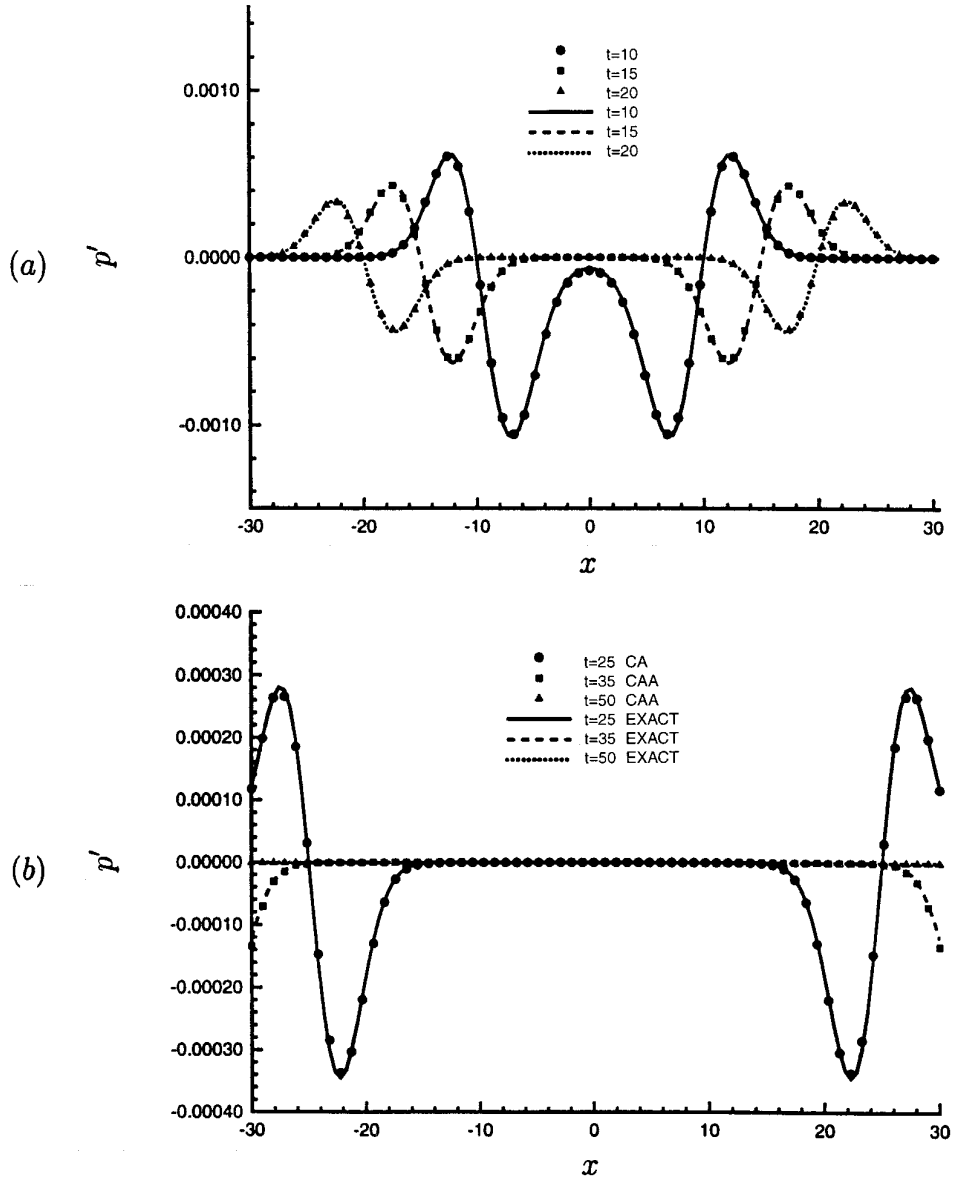

FIG. 3. Instantaneous acoustic pressure at different times for the spherical acoustic pulse problem in a stationary medium: (a) before the pulse begins to move out of the domain; (b) after the pulse begins to move out of the domain.

$t = 25$ while most of the wave has exited the computational domain at $t = 50$. Figure 6 indicates that there is no discernible numerical reflection from the boundaries.

The average magnitude of the pressure fluctuation $\langle |p'| \rangle$ and the average error in pressure $\langle |p' - p'_{\text{exact}}| \rangle$ at different times are shown in Fig. 7. After about $t = 80$, the acoustic wave has exited the computational domain and, therefore, these two average values are identical. This time is much larger than the corresponding time in the stationary medium ($t = 50$) due to convection. Similar to the pulse problem in the stationary medium, the average error, as well as the average of the pressure disturbance magnitude after the pulse, exits the domain is $\mathcal{O}(10^{-6})$. Furthermore, the magnitude of the pressure disturbance remains at this level after the pulse moves out of the domain, indicating no significant wave reflection from both the radiation and outflow boundaries.

5. AXISYMMETRIC JET SIMULATIONS

Calculations of the flow and noise radiation from a perfectly expanded, axisymmetric, unheated supersonic jet are shown in this section. The jet exit Mach number is 2.1 and the Reynolds number is 70,000. These flow conditions

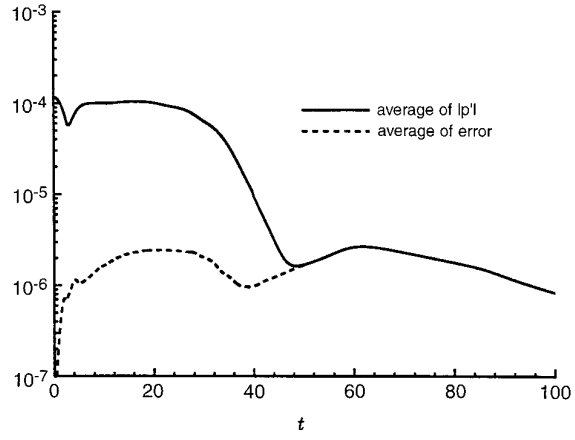

FIG. 4. The evolution of fluctuating pressure magnitude and error for the spherical acoustic pulse problem in a stationary medium.

correspond to the experiments of Troutt and McLaughlin [18], where experiments for both natural and excited jet conditions are reported for both flow and acoustic measurements.

5.1. Mean Flow Solution

As described above, the mean-flow solution has been obtained separately using a Reynolds averaged Navier–Stokes solver [9]. The computational grid used in the mean-flow calculation extends 70 radii in the axial direction and 10 radii in the radial direction. The mean jet calculations are performed on one azimuthal plane only by utilizing the axisymmetric nature of the mean flowfield. The grid has 264 points in the axial direction, 108 points in the radial direction, and 3 azimuthal planes. An algebraic turbulence model is used to model the Reynolds stresses. Figure 8 compares the predicted centerline Mach number with the experimental data. As shown in Fig. 8, the potential core length is predicted to be about 6 to 8 jet diameters. The potential core length, radial mean flow distribution and the spreading rate of the jet are some of the mean flow features that play an important role in the development of the turbulent structures and their subsequent Mach wave radiation. Hence, the mean flow quantities need to be computed accurately in order to obtain the correct farfield acoustic directivity and spectra. The centerline velocity decay agrees fairly well with the experimental result. Radial Mach number profiles at two axial locations are shown in Fig. 9 and they also compare well with the experiment. The computational grids used for the mean flow calculation and the aeroacoustic calculation are different. Hence, there is a need to interpolate the mean flow solution onto the aeroacoustic grid. This is performed with a second-order bilinear interpolation technique.

5.2. Computational Grid

Jet noise calculations could be performed either with Cartesian or polar grid systems. Uniform Cartesian grids are very expensive for three-dimensional aeroacoustic simulations due to the large number of grid points required and are impractical using present day computational technology. The next alternative is to use stretched Cartesian grids with more points near the shear layers and a relatively coarse grid in the far-field regions. However, as discussed in Morris *et al.* [19], the use of stretched Cartesian grids leads to nonuniform dispersion and dissipation errors in the azimuthal direction when applied to axisymmetric jet calculations. This problem of azimuthal nonuniformity may be rectified by the use of polar grid systems. Therefore, all the results shown in this paper employ stretched polar grids.

Extensive two-dimensional simulations have been performed to determine the grid requirements in the acoustic source and radiation regions. The polar grids used in the jet noise calculation are shown in Figs. 10 and 11 in axial and radial cross sections, respectively. The computational domain extends 70 jet radii in the axial direction and 40 jet radii in the radial direction. The grid for the aeroacoustic calculations has 280 points in the axial direction, 43 azimuthal planes, and 180 points in the radial direction. As shown clearly in Figs. 10 and 11, the grid is uniform in the axial and azimuthal directions, whereas it is stretched in the radial direction to put more points near the shear layer region. In particular, the grid points are concentrated on a radius $r = 1 + \beta x$, where $\beta = 0.05$ is used. That is, more points are placed at a radius equal to the jet radius at $x = 0$ while they are placed at a larger radius for further downstream locations, since the mixing layer grows with increasing downstream location. The number of grid points between $r = 0$ and $r = 1 + \beta x$ is 36. The stretching factor (defined as the ratio between adjacent grid spacing) is about 1.03 at $x = 0$ and 1.008 at $x/R_j = 70$. Figure 11 indicates that, near the jet exit, most of the grid points are placed within 10 jet radii while more points are located at larger radial distances further downstream.

5.3. Inlet Conditions

The inlet conditions are the unsteady flow perturbation conditions prescribed at the nozzle exit at every time step of the calculation. Previous experimental and numerical simulations [5, 18] have shown that the nozzle exit conditions can have a profound effect on the development of the jet. The exit conditions may affect the integrated features of the jet such as the potential core length, turbulence levels, and spreading rates. Troutt and McLaughlin's [18] experiment indicated that exciting the jet at a Strouhal number between 0.2 and 0.4 decreases the potential core length and increases the spreading rate when compared to

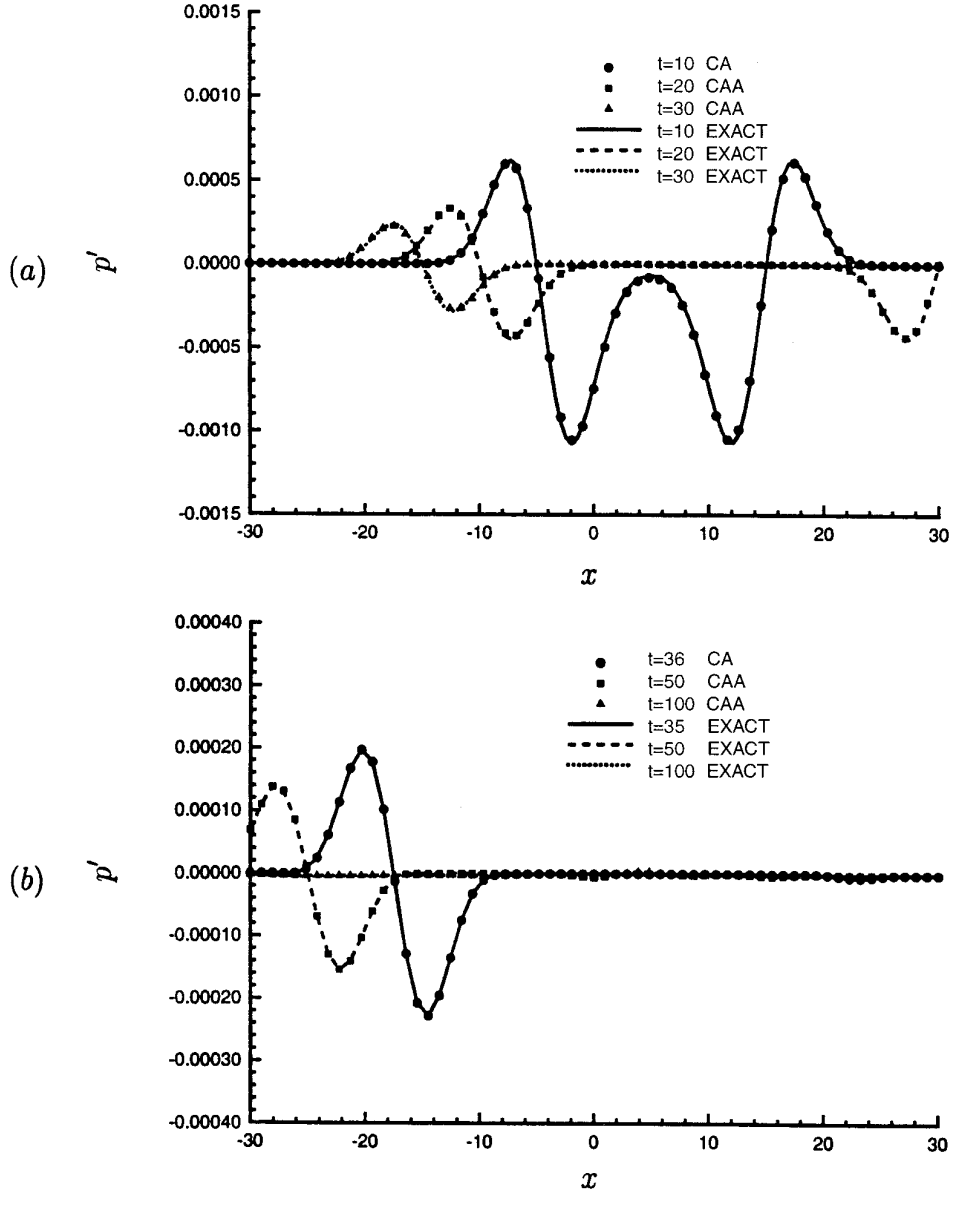

FIG. 5. Instantaneous acoustic pressure at different times for the spherical acoustic pulse problem in a moving medium: (a) before the center of the pulse moves out of the domain; (b) after the center of the pulse moves out of the domain.

the natural jet case. Also, the far-field noise amplitude levels increase due to the excitation. However, they found that the acoustic directivity was similar to the natural jet case. Due to experimental constraints they were unable to measure the unsteady nature of the perturbations, such as their temporal behavior and phase content at the nozzle exit.

It has been well established that large-scale structures play a dominant role in the noise generation process of supersonic jets [20]. Experimental investigations by Troutt and McLaughlin [18] for moderate Reynolds number cold jets and by Seiner *et al.* [20] for high Reynolds number jets have shown that the coherent large-scale structures are efficient noise generators and that they may be considered as a superposition of instability waves. Hence, the present numerical jet simulations attempt to simulate the nozzle exit conditions as a superposition of instability waves. The spatial and temporal development of the instability wave in the shear layer depends on the excitation frequency which, in turn, affects the Mach wave radiation. In this paper, three types of inlet conditions have been implemented and the subsequent development of the perturbation field is discussed in the following sections.

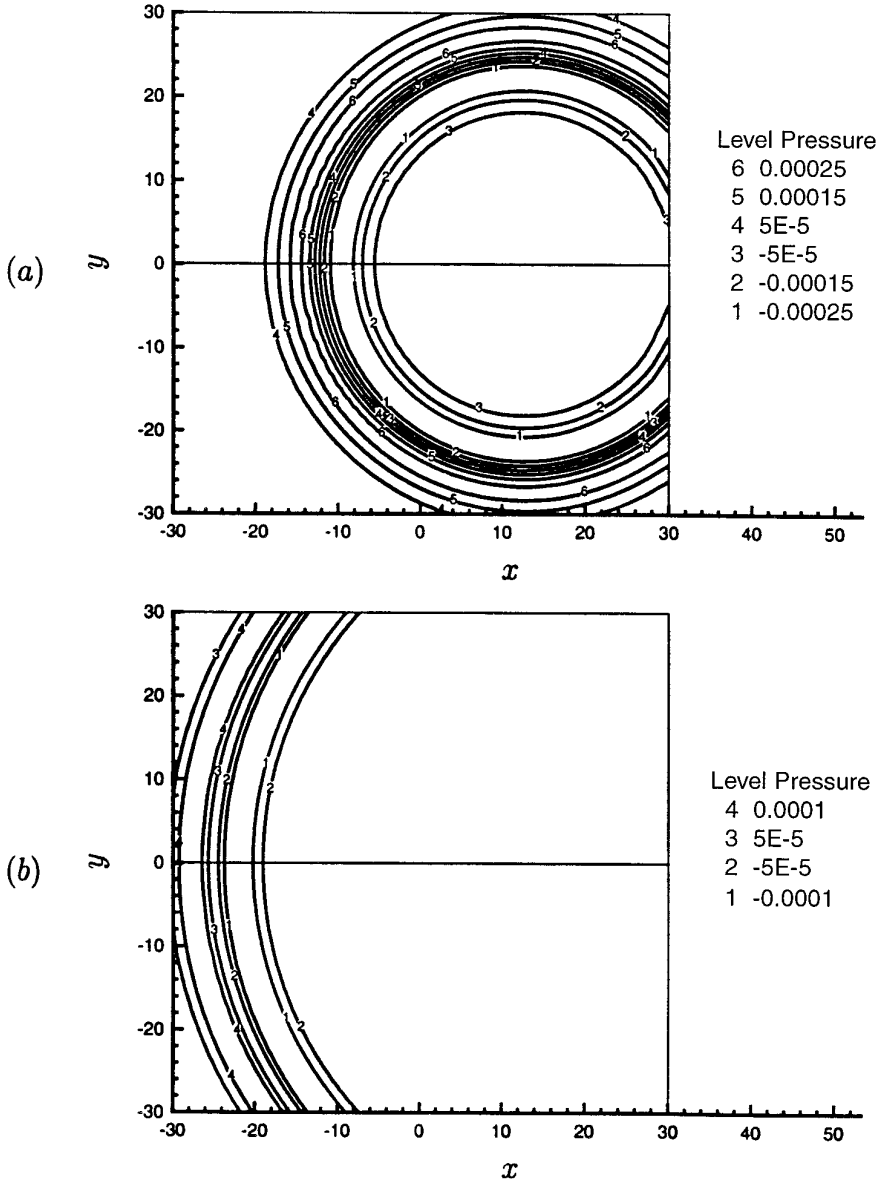

FIG. 6. Acoustic pressure contours for the moving spherical pulse in x-direction with flow Mach number of 0.5: (a) $t = 25$; (b) $t = 50$.

5.3.1. *Axisymmetric Inlet Conditions*

Under these inlet conditions, the flow perturbations at the nozzle exit are specified as axisymmetric perturbation eigenfunctions at a Strouhal number of 0.2. These eigenfunctions are calculated from a linear stability analysis [21]. The form of the perturbation flow vector is given by

$$\begin{Bmatrix} \rho' \\ u_x' \\ u_r' \\ u_\theta' \\ p' \end{Bmatrix} = \varepsilon \mathrm{Re} \begin{Bmatrix} \hat{\rho}' \\ \hat{u}_x' \\ \hat{u}_r' \\ 0 \\ \hat{p}' \end{Bmatrix} \exp(-i\omega t). \tag{23}$$

The ^ quantities in density, velocity components, and pressure are the complex eigenfunctions given by the linear theory; u_x', u_r', and u_θ' are the perturbation velocities in the axial, radial, and azimuthal directions respectively; ε is the amplitude which is set equal to 1.0e $-$ 03; ω is the radian frequency of the excitation.

Three-dimensional simulations have been performed in parallel using up to 28 IBM-SP2 processors. The equivalent single processor CPU time would be about 1500 h; however, the nearly ideal scalability of the present code reduces this time by a factor of up to 28. Axisymmetric mode calculations have been performed by other researchers [8, 5, 9] using a two-dimensional grid and utilizing the axisymmetric nature of all flow quantities. In the present

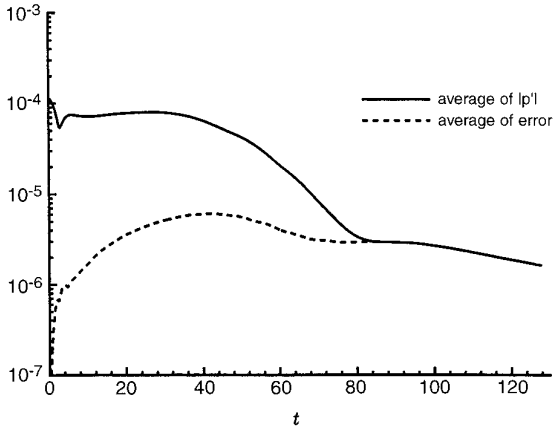

FIG. 7. The evolution of fluctuating pressure magnitude and error for the spherical acoustic pulse problem in a moving medium.

work, however, three-dimensional calculations are performed even for the axisymmetric mode. The present CAA code is capable of handling arbitrary spatial and temporal variations of the perturbation quantities at the nozzle exit. As expected, for these initial conditions, axisymmetric near and far-field solutions are obtained as part of the solution.

Figure 12 shows the sound pressure level (SPL) contours on an axial cross section of the jet. No significant reflections are seen either at the radiation boundaries or at the outflow boundary. The decibel levels are matched to the experimental data at one location corresponding to 45 radii in the axial direction and 20 radii in the radial direction. A highly directional directivity pattern is observed in the contour plot. As expected, the strongest acoustic source region is near the end of the potential core. The peak angle of radiation is about 22° from the jet axis. Troutt and McLaughlin [18] reported a peak radiation angle of 25° from the jet axis for the excited jet at a Strouhal number of 0.2; however, they found that the azimuthal character of the disturbance was a combination of axisymmetric and helical modes. Figure 13 shows a cross section of the experimental SPL contours obtained by Troutt and McLaughlin [18]. A radial cross section of the SPL contours at a downstream distance of 50 radii is shown in Fig. 14. The axisymmetric nature of the perturbation field is preserved throughout the domain. Figure 15 shows the amplitude evolution of the perturbation pressure wave in the jet shear layer (at the nozzle lip line). The root mean square (RMS) pressure shows an exponential increase in amplitude until $x/R_j = 15.0$ and then a gradual decay. This is consistent with the weakly nonlinear calculations of Tam and Burton [4].

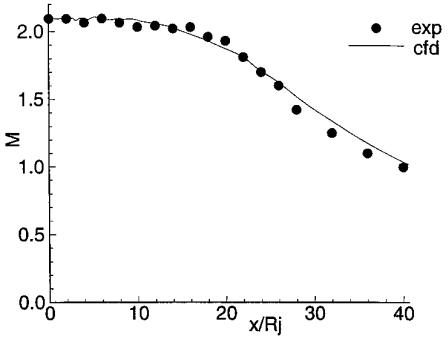

FIG. 8. Centerline Mach number distribution compared to Troutt and McLaughlin's [18] experimental data.

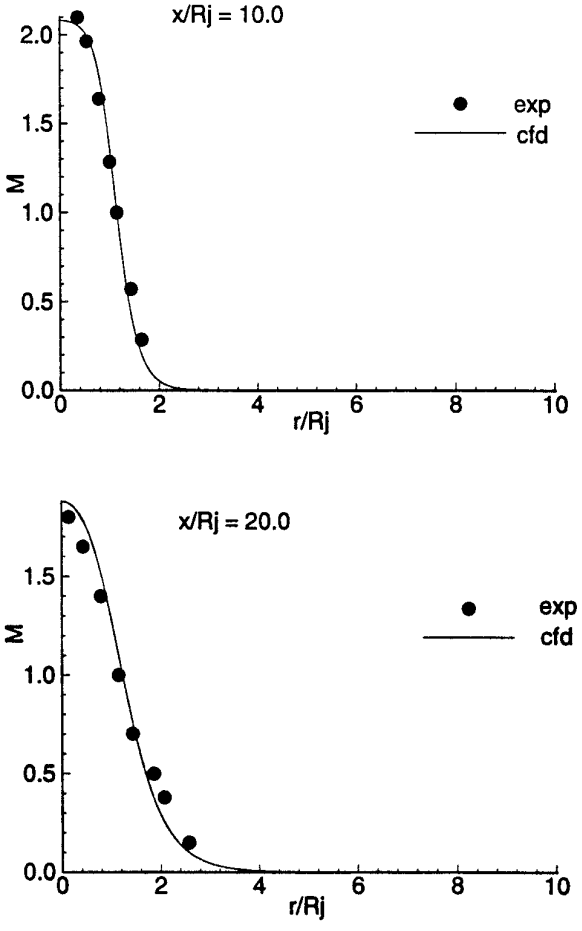

FIG. 9. Radial Mach number distribution at $x/R_j = 10.0$ and $x/R_j = 20.0$. Experimental data by Troutt and McLaughlin [18].

5.3.2. *Helical Inlet Conditions*

Previous analytical studies (Morris and Tam [3], Tam and Burton [4]) have shown that the first helical mode ($n = \pm 1$) is the most amplified mode in supersonic jets with Mach number above 1.4. Troutt and McLaughlin's experiment [18] also indicates that the helical mode dominates in the Strouhal number range of 0.2–0.4. In order to excite the helical mode in the present numerical approach, the helical nature of the disturbance is prescribed at the

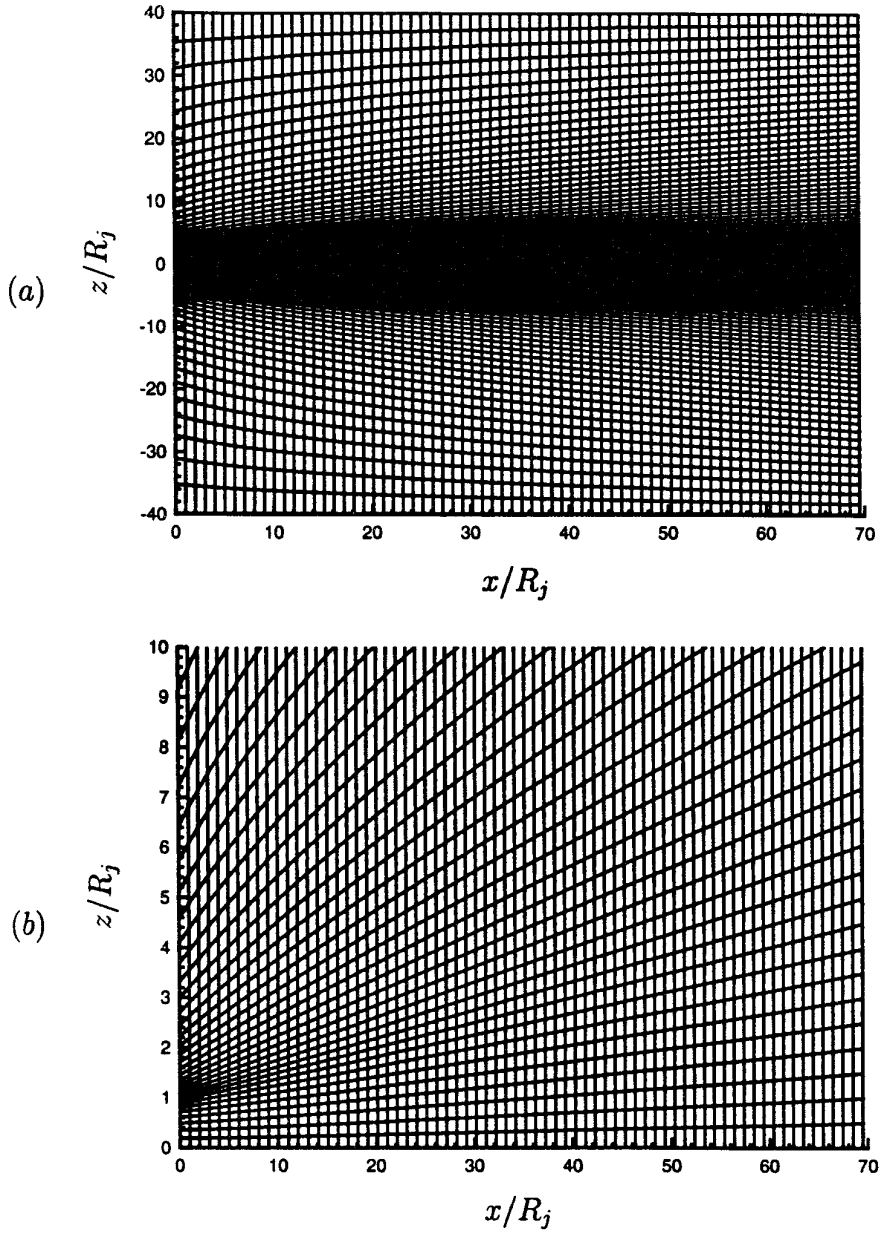

FIG. 10. The axial cross section of the polar grid used in the jet noise calculation (every fourth grid point shown): (a) the whole computational domain; (b) part of the computational domain for $r/R_j < 10$.

nozzle exit. The corresponding mathematical form of the flow variables at the nozzle exit is given by

$$\begin{Bmatrix} \rho' \\ u'_x \\ u'_r \\ u'_\theta \\ p' \end{Bmatrix} = \varepsilon \mathrm{Re} \begin{Bmatrix} \hat{\rho}' \cos\theta \\ \hat{u}'_x \cos\theta \\ \hat{u}'_r \cos\theta \\ \hat{u}'_\theta \sin\theta \\ \hat{p}' \cos\theta \end{Bmatrix} \exp(-i\omega t); \qquad (24)$$

θ represents the azimuthal angle in the cross-sectional plane. This form represents a superposition of the ± 1 helical modes. The perturbation eigenfunctions are calculated using linear stability theory for a Strouhal number of 0.2 and an analytical mean flow profile [21]. The helical perturbations are prescribed at the nozzle exit at each time step. The instability waves amplify in the initial core region and saturate in magnitude at an axial distance of 20.0 radii at $St = 0.2$. The instantaneous pressure disturbance and the RMS pressure variation along the nozzle lip line at $\theta = 0°$ are shown in Fig. 16. The initial amplitude for this case is

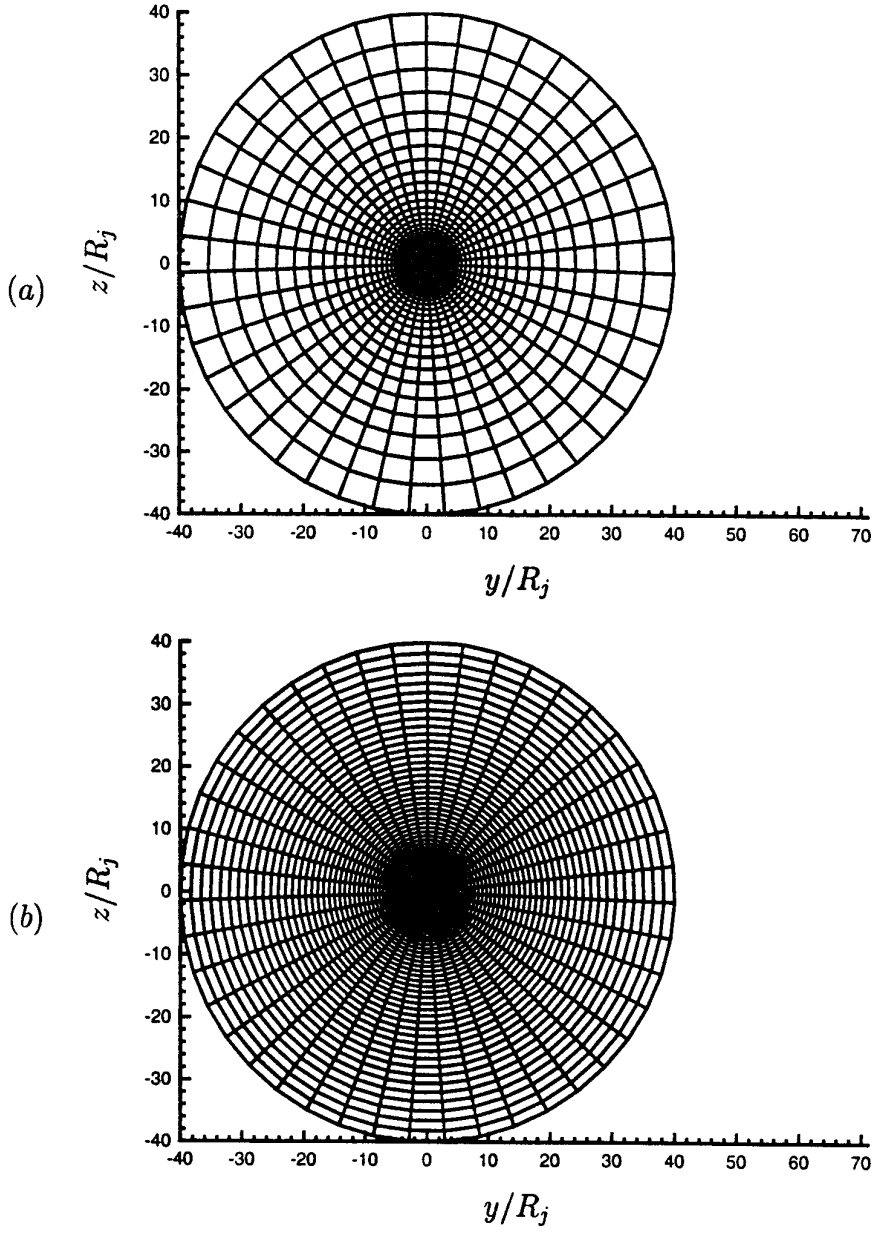

FIG. 11. The radial cross section of the polar grid used in the jet noise calculation (every fourth grid point shown in the radial direction): (a) $x/R_j = 0$; (b) $x/R_j = 70$.

chosen to be 1.0e − 05. The axial cross section of the SPL contours in the x-y plane are shown in Fig. 17. The peak radiation is predicted at an angle of 18° to the jet axis measured from the nozzle exit. As expected, the peak radiation angle is less than that seen in the axisymmetric mode case. This is consistent with the linear theory that predicts that the helical mode has a lower phase velocity than the axisymmetric mode. However, the computations predict lower peak angles when compared to the experiment. This discrepancy may be due to some inaccuracies in the mean flow predictions, especially up to the end of the potential core region, the radial distribution of the mean flow and the spreading rate. The measured acoustic spectra show considerable energy content in the higher harmonics and a significant percentage of energy in the broadband frequencies. However, in the present numerical simulation, the harmonic input generates a harmonic far-field. This is because of the small initial amplitude of the disturbance, much lower than Troutt and McLaughlin's [18] experimental values. Hence, there is a significant difference between the frequency content of the measured spectra and the numerical simulation which may result in

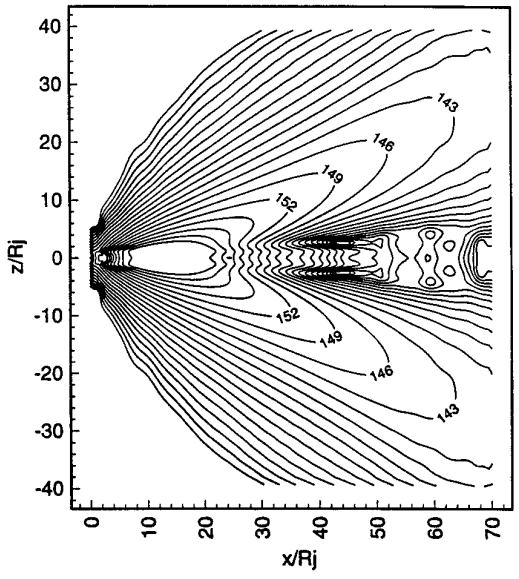

FIG. 12. Axial cross section of sound pressure level (dB) contours, $y/R_j = 0.0$. Axisymmetric, harmonic time input, $St = 0.2$.

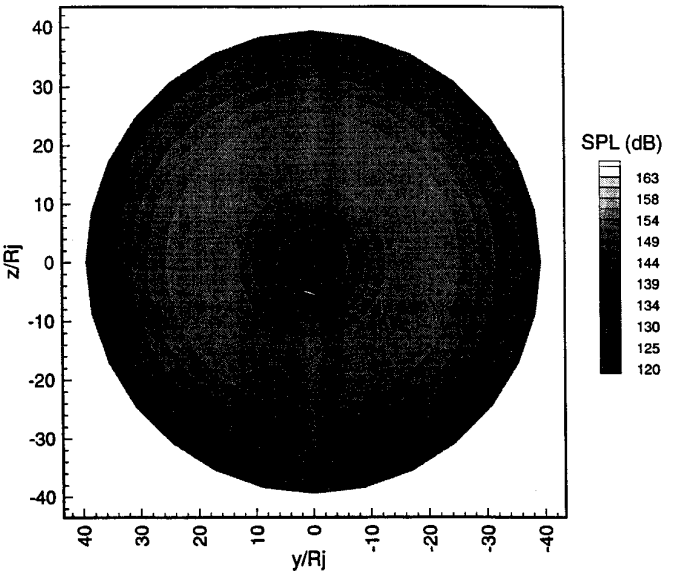

FIG. 14. Sound pressure level (dB) contours at a radial section, $x/R_j = 50.0$. Axisymmetric, harmonic input, $St = 0.2$.

the differences in the directivity. A typical radial cross section of the SPL contours at $x/R_j = 50.0$ are shown in Fig. 18. The azimuthal variation seen in Fig. 18 is typical of a sum of the ± 1 helical modes.

5.3.3. *Random Inlet Conditions*

In this case the objective is to specify the inlet perturbations at the nozzle exit in a random fashion both temporally and spatially. This is done to simulate the natural jet exit conditions as closely as possible. The spatial distributions are chosen to be a combination of the axisymmetric and the ± 1 helical modes. The axis of symmetry of the ± 1 helical modes is chosen at random at each time step. The temporal variation of the perturbations are chosen using a random walk approach [7]. The basis of this approach is to add a random component to the phase of a base frequency resulting in a shifting of the energy content to the neighboring frequencies. This approach can be used to tailor the input spectral content as desired to match available experimental data.

In the present case, the input spectrum has a broadband frequency distribution centered around $St = 0.6$. It is shown as the $x/R_j = 0.0$ spectrum in Fig. 22 below. The radial

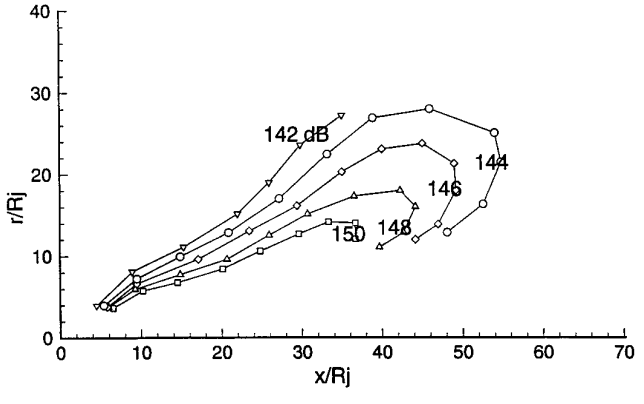

FIG. 13. Axial cross section of sound pressure level (dB) contours. Troutt and McLaughlin's experimental data.

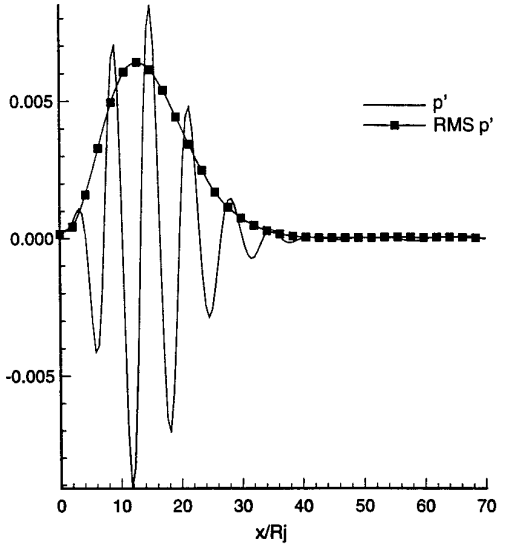

FIG. 15. Pressure wave amplitude evolution along the nozzle lip line. Axisymmetric, harmonic input, $St = 0.2$.

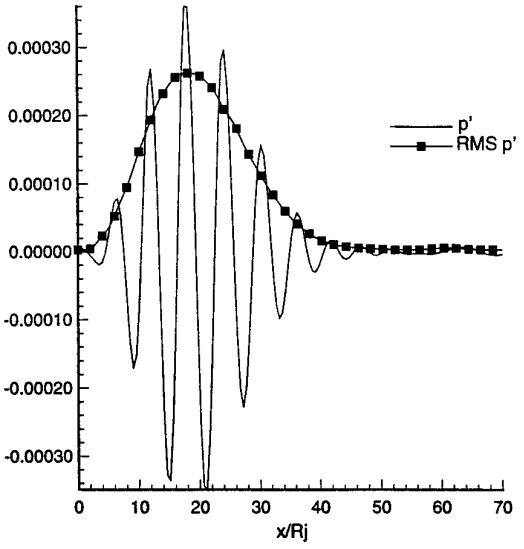

FIG. 16. Pressure wave evolution at the nozzle lip line. Helical, harmonic input, $St = 0.2$.

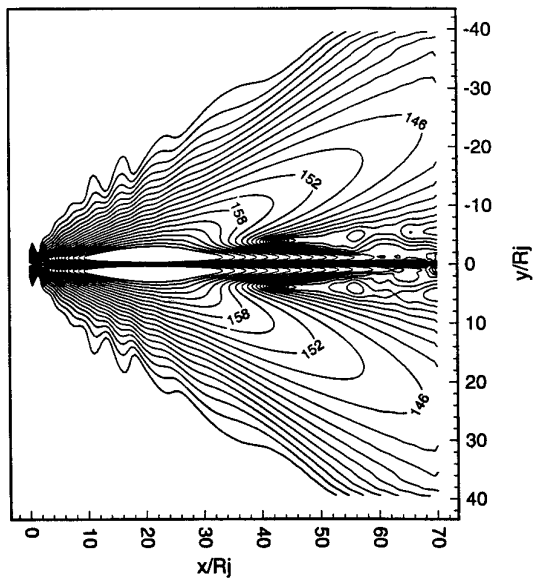

FIG. 17. Axial cross section of sound pressure level (dB) contours, $z/R_j = 0.0$. Helical, harmonic input, $St = 0.2$.

distribution of the perturbation variables at the nozzle exit is chosen to be a Gaussian distribution centered around the nozzle lip line with a half-width equal to 2% of the jet radius. Similar Gaussian distributions have been chosen by other researchers in their jet calculations [7]. The form of the perturbations at the nozzle exit is given by

$$\begin{Bmatrix} \rho' \\ u_x' \\ u_r' \\ u_\theta' \\ p' \end{Bmatrix} = \varepsilon \begin{Bmatrix} \hat{\rho}'(1+\cos(\theta+\psi)) \\ \hat{u}_x'(1+\cos(\theta+\psi)) \\ \hat{u}_r'(1+\cos(\theta+\psi)) \\ \hat{u}_\theta' \sin(\theta+\psi) \\ \hat{p}'(1+\cos(\theta+\psi)) \end{Bmatrix} \exp(-i(\omega t+\phi)). \quad (25)$$

Here the ^ quantities in density, velocity components, and pressure are the Gaussian distributions in the respective quantities. In Eq. (25), ψ is the random component of the azimuthal angle for the axis of the helical distribution and ϕ is the random phase added to the base frequency ω. In particular, these two angles at time steps $n+1$ are obtained from their values at the previous time step n as

$$\phi^{n+1} = \phi^n \pm \Delta\phi, \quad \psi^{n+1} = \psi^n \pm \Delta\psi, \quad (26)$$

where $\Delta\phi = 0.015 = 5.4°$ and $\Delta\psi = 0.030 = 10.8°$. The signs in Eq. (26) are chosen in a random manner and may differ between two adjacent time steps. At the first time step $\phi^1 = \psi^1 = 0$. To obtain a broadband spectra, the base frequency ω is taken as a sum of discrete frequencies with different random phase components. In the present calculation, the Strouhal numbers for the base frequencies are chosen to be 0.2, 0.45, and 0.7 with individual random phase additions.

Figure 19 shows an axial cross section of the SPL contours in the x-y plane. In this case the peak radiation angle is found to be 24°. The experimental measurements of Troutt and McLaughlin [18] in the natural jet case gave 25°. The random nature of the time dependent pressure

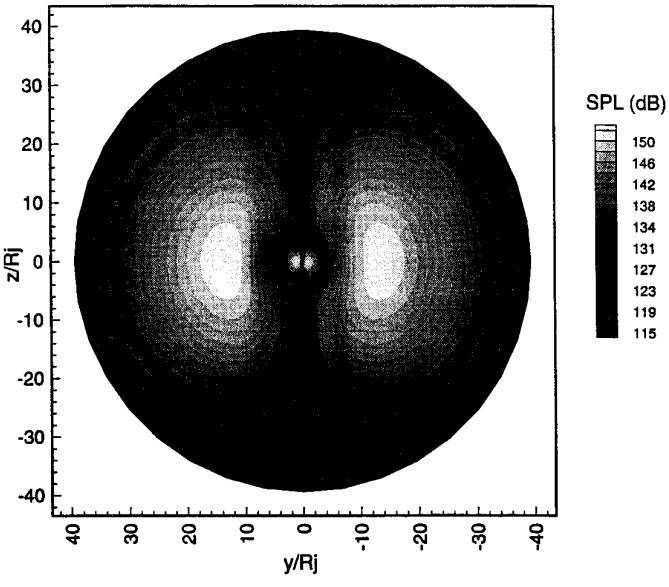

FIG. 18. Sound pressure level (dB) contours at a radial section, $x/R_j = 50.0$. Helical, harmonic input, $St = 0.2$.

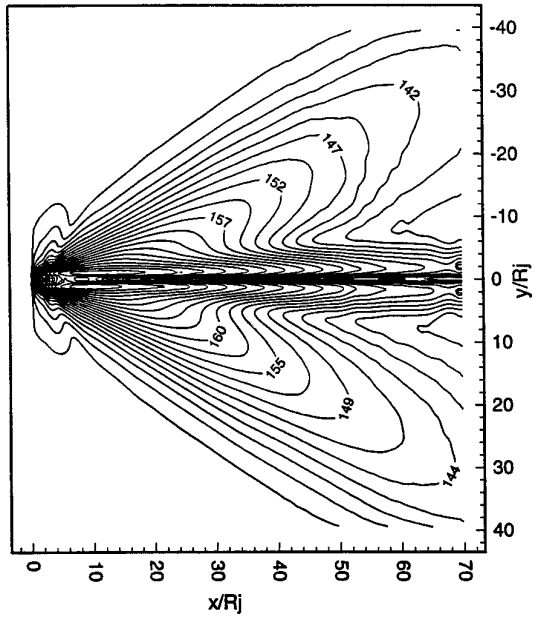

FIG. 19. Axial cross section of sound pressure level (dB) contours, $z/R_j = 0.0$. Random inlet conditions.

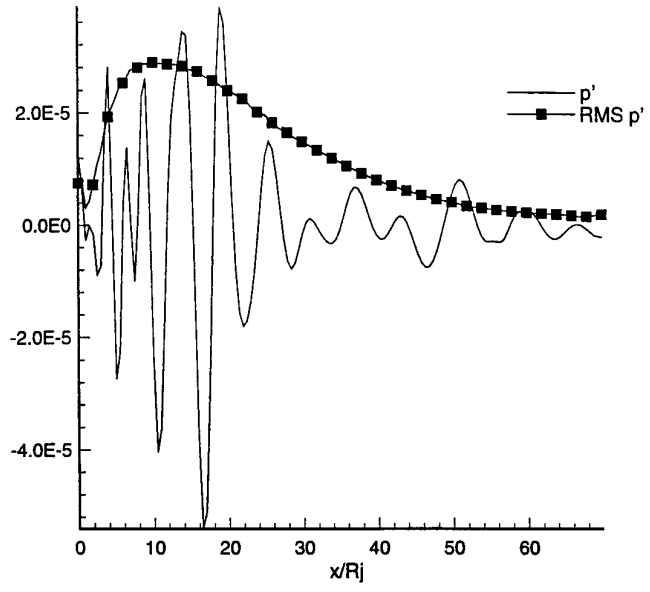

FIG. 21. Axial variation of instantaneous perturbation pressure and RMS pressure along the nozzle lip line, $\theta = 0°$. Random inlet conditions.

field can be observed in the instantaneous pressure plots; however, there is a preferred Mach wave radiation originating from the jet shear layer in the potential core region. The radial cross-sectional SPL contours are shown at $x/R_j = 50.0$ in Fig. 20. The averaged pressure contours exhibit a nearly axisymmetric nature in both the near and far-fields. The RMS values are expected to be axisymmetric in nature. In the numerical simulations, the jet flaps along a random orientation at any given instant. A typical pressure wave amplitude evolution on the jet lip line is shown in Fig. 21. It is interesting to note that, although the initial conditions are broadband, the instantaneous pressure distribution shows a quasi-periodic spatial structure. This is evidence of the selective amplification properties of the jet mean flow. The RMS pressure variation is also shown in Fig. 21. As expected, the RMS value is seen to increase exponentially in the initial core region and then decay gradually.

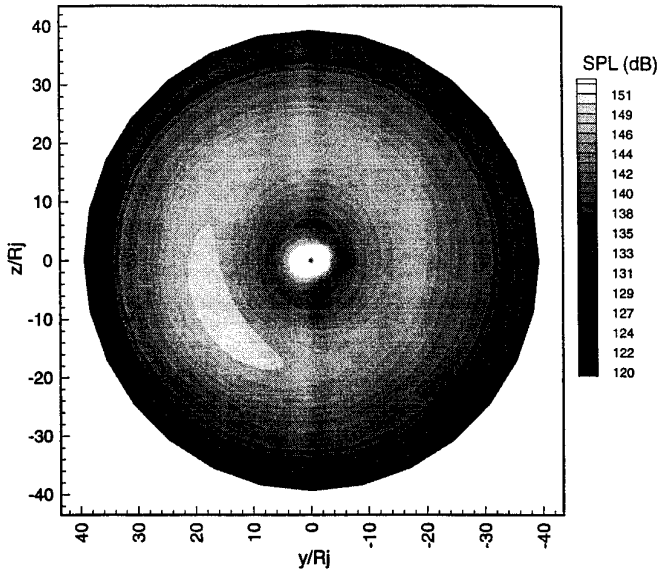

FIG. 20. Sound pressure level (dB) contours at a radial section, $x/R_j = 50.0$. Random inlet conditions.

Since the inlet conditions are broadband, the instability waves with different frequencies are expected to grow and saturate with different growth rates and at different axial locations. The acoustic spectra in the maximum radiation direction are expected to peak at the frequency of the most amplified wave, assuming that it is convecting supersonically. Figure 22 shows the perturbation pressure spectra at several downstream locations on the jet lip line. As noted in Troutt and McLaughlin's [18] experiments, the peak frequency in the spectra shifts towards lower values with downstream distance. At $x/R_j = 10.0$, the instability wave with $St = 0.4$ reaches the maximum amplitude and starts to decay. Similarly, the $St = 0.2$ wave peaks at $x/R_j = 20.0$ and so on. Low frequency flapping of the jet is seen at the downstream locations. This flapping is also reflected in the averaged flowfield as the time sampling is performed over 10,000 time steps which translates to only a few periods of the low frequency oscillation.

The far-field acoustic spectrum in the direction of maximum radiation is shown in Fig. 23. The far-field spectrum

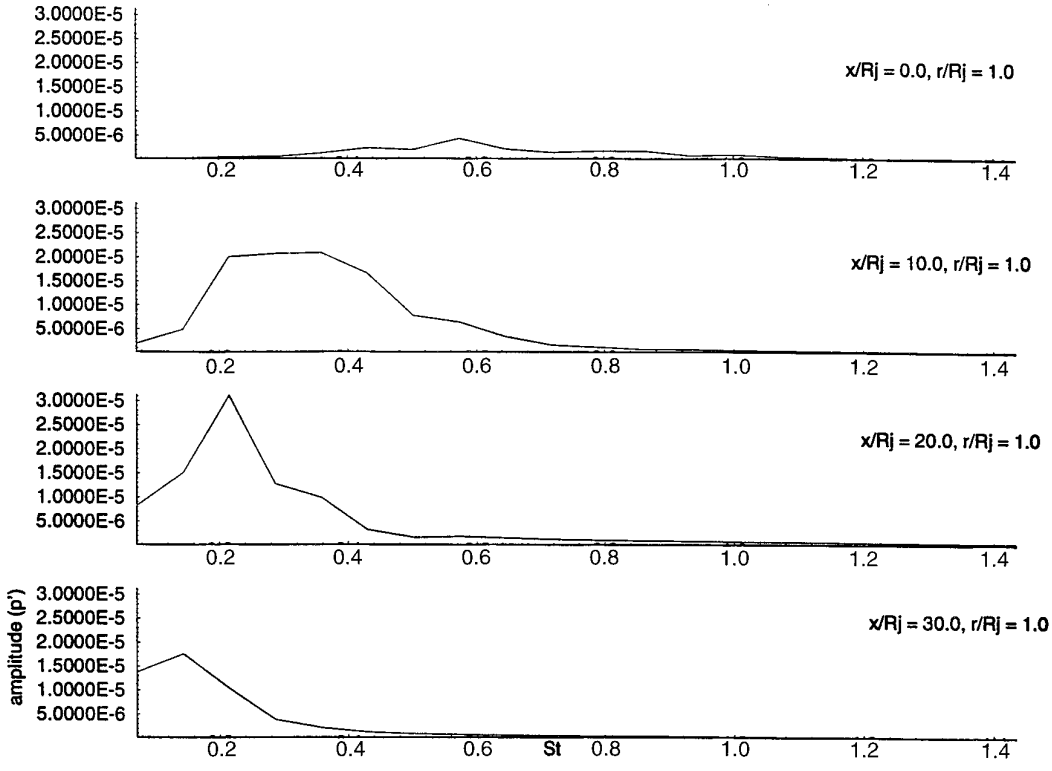

FIG. 22. Pressure spectra along the nozzle lip line at several axial locations. Random inlet conditions.

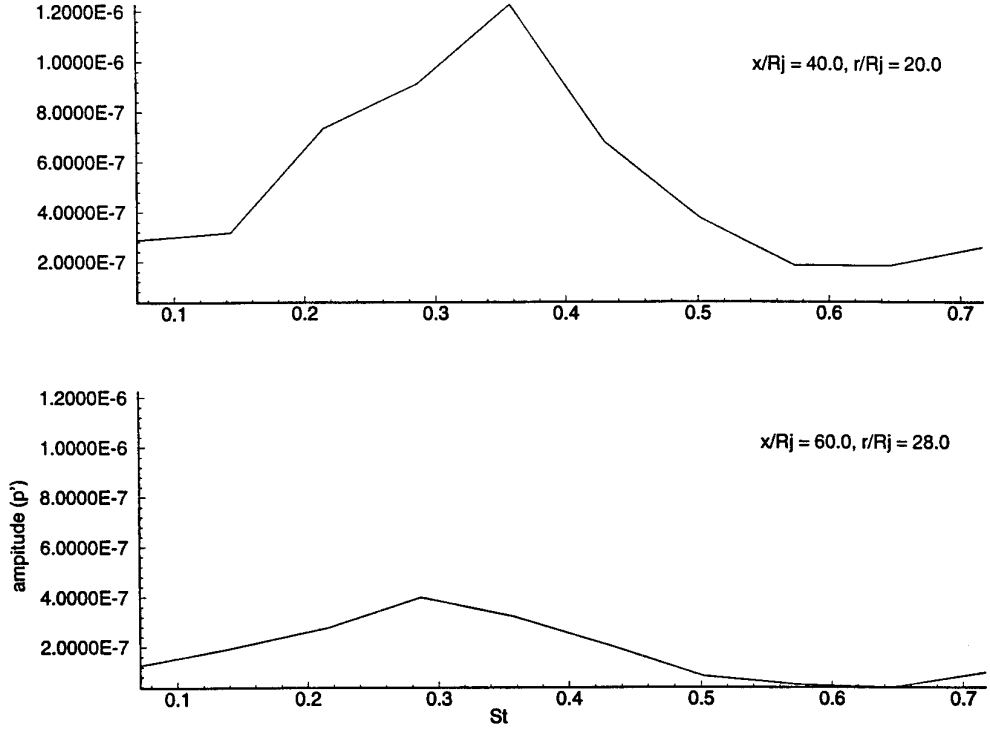

FIG. 23. Pressure spectra along the maximum radiation direction. Random inlet conditions.

shows a peak at a Strouhal number of approximately 0.3. This selection of a dominant radiation frequency has been observed in moderate Reynolds number supersonic jet experiments [18] and also in high Reynolds number hot jet experiments [20]. The far-field computational grid cannot resolve beyond a Strouhal number of 0.7 and, hence, the far-field spectrum is not computed beyond this value. In this random inlet jet simulation, the frequency selection mechanism of the natural jet and the instability wave amplitude evolution at different Strouhal numbers have been reproduced.

6. CONCLUDING REMARKS

A three-dimensional CAA code has been developed to analyze the acoustic radiation characteristics of jet flows. The solution procedure is more robust than the LES or DNS approaches. This makes it possible to increase the size of the computational domain to include farfield regions which would not be practical using the full Navier–Stokes methods. Excellent parallel performance has been achieved. Three-dimensional test problems have been solved and compared with exact solutions. Axisymmetric jet noise calculations have been performed under different inlet conditions using large scale computational grids. The acoustic directivity and spectra compare well with the experimental data. In this paper it has been demonstrated that practical three-dimensional jet noise problems may be solved accurately and efficiently using the non-linear disturbance equations and parallel computers.

ACKNOWLEDGMENTS

This work has been supported by NASA Langley Research Center under task order NAS1-20102. The technical monitor is Mr. R. A. Golub. The program is administered by Lockheed Martin Aeronautical Systems Corporation. The project manager is Dr. N. N. Reddy. The authors acknowledge the help of Dr. L. N. Sankar and Dr. K. Viswanathan who provided the RANS mean-flow solutions.

REFERENCES

1. M. J. Lighthill, *Proc. R. S. London* **211,** 564 (1952).
2. G. M. Lilley, AFAPL-TR-72-53, 1972 (unpublished).
3. P. J. Morris and C. K. W. Tam, On the radiation of sound by instability waves of a compressible axisymmetric jet, in *Mechanics of Sound Generation in Flows* (Springer-Verlag, Berlin, 1979), p. 55.
4. C. K. W. Tam and D. E. Burton, *J. Fluid Mech.* **138,** 273 (1984).
5. R. Hixon, S. H. Shih, and R. R. Mankbadi, CEAS/AIAA Paper 95-116, 1995 (unpublished).
6. R. R. Mankbadi, M. E. Hayder, and A. Povinelli, *AIAA J.* **32,** 897 (1994).
7. T. S. Chyczewski and L. N. Long, AIAA Paper 96-1730, 1996; *J. Comput. Phys.,* submitted.
8. B. E. Mitchell, S. K. Lele, and P. Moin, Direct computation of the sound generated by subsonic and supersonic axisymmetric jets, Technical Report TF-66, Stanford University, 1995 (unpublished).
9. K. Viswanathan and L. N. Sankar, *AIAA J.* **33,** 2271 (1995).
10. J. C. Hardin and D. S. Pope, in *Proceedings, DGLR/AIAA 14th Aeroacoustics Conference, AIAA, Washington, DC, 1992,* p. 448.
11. J. C. Hardin and D. S. Pope, *AIAA J.* **33,** 407 (1995).
12. K. A. Hoffmann, *Computational Fluid Dynamics for Engineers* (Engineering Education System, Austin, Texas, 1989).
13. F. Q. Hu, M. Y. Hussaini, and J. L. Manthey, *J. Comput. Phys.* **124,** 177 (1996).
14. C. K. W. Tam and J. C. Webb, *J. Comput. Phys.* **107,** 262 (1993).
15. C. K. W. Tam, AIAA Paper 95-0677, 1995 (unpublished).
16. A. Bayliss and E. Turkel, *J. Comput. Phys.* **48,** 182 (1982).
17. S. H. Shih, R. Hixon, and R. R. Mankbadi, AIAA Paper 95-0681, 1995 (unpublished).
18. T. R. Troutt and D. K. McLaughlin, *J. Fluid Mech.* **116,** 123 (1982).
19. P. J. Morris, L. N. Long, A. Bangalore, T. Chyczewski, D. P. Lockard, and Y. Ozyoruk, Experiences in the practical application of computational aeroacoustics, FED, Vol. 238, "Proceedings, ASME Fluids Engineering Conference, Vol. 3, 1996."
20. J. M. Seiner, D. K. McLaughlin, and C. H. Liu, NASA TP 2072, 1982 (unpublished).
21. C. M. Shieh, Master's thesis, Pennsylvania State University, 1995 (unpublished).